Title page

Effect of colloidal particle size on physicochemical properties and aggregation behaviors of two alkaline soils

Yu-yang Yan[1], Xin-ran Zhang[1], Chen-yang Xu[1,2]*, Jun-jun Liu[1], Fei-nan Hu[3,4], Zeng-chao Geng[1,2]

(1. *College of Natural Resources and Environment*, *Northwest A&F University*, *Yangling*, *Shaanxi* 712100, *China*; 2. *Key Laboratory of Plant Nutrition and the Agri-environment in Northwest China, Ministry of Agriculture, Northwest A&F University, Yangling, Shaanxi 712100, China; 3. State Key Laboratory of Soil Erosion and Dryland Farming on the Loess Plateau, Northwest A&F University, Yangling, Shaanxi 712100, China; 4. Institute of Soil and Water Conservation, Chinese Academy of Sciences, Ministry of Water Resources, Yangling, Shaanxi 712100, China*)

***Corresponding author:**

Chen-yang Xu

Email address: xuchenyang@nwafu.edu.cn, xuchenyang.ms@163.com;

Postal address: College of Natural Resources and Environment, Northwest A&F University, No. 3 Taicheng Road, Yangling District, Shaanxi 712100, China.

Abstract

Colloidal particles are the most active soil components, and they vary in elemental composition and environmental behaviors with the particle size due to the heterogenous nature of natural soils. The purposes of the present study are to clarify how particle size affects the physiochemical properties and aggregation kinetics of soil colloids, and to further reveal the underlying mechanisms. Soil colloidal fractions, from two alkaline soils—Anthrosol and Calcisol were subdivided into three ranges: $d < 2$ μm, $d < 1$ μm and $d < 100$ nm. The organic and inorganic carbon contents, clay mineralogy, surface electrochemical properties, including surface functional groups and zeta potentials, were characterized. Through time-resolved light scattering technique, the aggregation kinetics of soil colloidal fractions were investigated, and their critical coagulation concentrations (CCCs) were determined. With decreasing colloidal particle diameter, the total carbon content, organic carbon, organic functional groups content and illite content all increased. The zeta potential became less negative and the charge variability decreased with decreasing particle diameter. The CCC values of Anthrosol and Calcisol colloids followed the descending order of $d < 100$ nm, $d < 1$ μm, $d < 2$ μm. Compared with the course factions ($d < 1$ μm and $d < 2$ μm), soil nanoparticles were more abundant in organic carbon and more stable clay minerals ($d < 100$ nm), thus they exhibited strongest colloidal suspension stability. The differences in organic matter contents and clay mineralogy are the fundamental reasons for the differences in colloidal suspension stability behind the size effects of Anthrosol and Calcisol colloids. The present study revealed the size effects of two alkaline soil colloids on carbon content, clay minerals,

surface properties and suspension stability, emphasizing that soil nanoparticles are prone to be more stably dispersed instead of being aggregated. These findings can provide references for in-depth understanding of the environmental behaviors of the heterogeneous soil organic-mineral complexes.

Keywords: Nanoparticles; Clay mineral composition; zeta potential; Critical coagulation concentration

1. Introduction

Soils contain a series of solid particles in continuous sizes, ranging over six orders of magnitude from nanometers to millimeters (Lead and Wilkinson, 2006; Li et al., 2011), among which soil colloids are the most reactive fractions. Soil colloids are characterized by high surface area and abundant surface charges, exhibiting high potential for carbon sequestration and strong adsorption capacity, which can largely determine the fate and transport of pathogens, nutrients, heavy metals and organic pollutants, and might cause environmental problems to adjacent water bodies or groundwater (Baalousha et al., 2009; Calabi-Floody et al., 2011). Due to their high reactivity and fluidity in aqueous environment, soil colloids play an important role in physical, chemical and biogeochemical processes in natural environment (Schäfer et al., 2012; Mayordomo et al., 2016). The capacity of soil colloids in mobilizing bound nutrients and pollutants is closely related to their dispersion stability under various environmental conditions (Won and Burns, 2018). Therefore, studies on the dispersion stability of soil colloids have attracted extensive attention.

Currently, the definition of soil and environmental colloidal fractions is ambiguous. Soil colloidal fractions are defined as soil particles in diameter of < 1 μm (Lead and Wilkinson, 2006; Weil and Brady, 2016), and also being of < 2 μm (Zhang et al., 2021); while in some extreme cases, they can refer to the particles in diameter of 5–10 μm (Yin et al., 2010). Such discrepancies are seen among publications due to the fact that colloids are defined based on the particle diameter range within which they can display colloidal properties. Since for different materials, e.g., metal (Fe/Al/Ti) oxides, silica

gel, phyllosilicates, the specific colloidal range differs greatly.

Compared with engineered nanoparticles with known mineralogical organization, natural soils are much more heterogeneous (Cárdenas et al., 2010); their elemental composition and clay mineralogy of soil colloids change with particle size. Tsao et al., (2013) found that quartz and feldspar were mainly dominant in colloidal particles of < 2 μm and 450–2000 nm in red soil (Ferralsols, WRB, IUSS Working Group WRB. 2022), while illite and montmorillonite were the main clay minerals in nanoparticles (1–100 nm). In addition, the mineral structure at nanometer scale also changes. Compared with colloidal particles of < 2 μm, the Si/Al ratio in nanoparticles increased, and the surface area, morphology, crystallinity, surface atomic structure and frame structure were significantly different (Tsao et al., 2011). Furthermore, particle size also affects the surface potential of soil colloids. Tang et al., (2015) investigated the surface potential variations with particle size (1–10 μm, 0.5–1 μm, 0.2–0.5 μm, < 0.2 μm) for variably-charged yellow soil (Lixisols) and permanently-charged purple soil (Leptosols); among the colloidal fractions, the absolute surface potential of the finest particles of purple soil (Leptosols) was lowest while that of the yellow soil (Lixisols) was the largest, caused by the differences in surface charge density. Thus, the influences of particle size on elemental composition and surface properties of soils should be further studied.

In recent years, great progress has been made in the study of dispersion stability of soil clay minerals, such as montmorillonite, kaolinite, illite or hematite, and soil nanoparticles (Xu et al., 2018; Sun et al., 2020; Wei et al., 2021; Zhu et al., 2014). He

et al., (2008) demonstrated that hematite nanoparticles with various particle diameters showed different surface properties and aggregation behaviors under the same pH conditions; moreover, the critical coagulation concentrations (CCCs) of hematite decreased with the decrease of particle diameter. Zhou et al., (2013) compared the CCCs of ten different TiO_2 nanoparticles with varying sizes and indicated that crystal structure and particle diameter both affected the aggregation behaviors of TiO_2. Zhang et al. (2016) confirmed that the types of clay minerals for two Alfisols changed from smectite and vermiculite to kaolinite and illite when the particle size varied from colloids to nanoparticles. Therefore, the dependence of physiochemical properties, surface properties and environmental behaviors on particle size for heterogeneous soil colloidal particles needs systematic investigation.

In the present study, soil colloidal particles of two alkaline soils—Anthrosol sand Calcisols were subdivided into three ranges: $d < 2$ μm, $d < 1$ μm and $d < 100$ nm. Their organic fraction and clay mineralogy, surface electrochemical properties and colloidal stability were studied. This study selected two representative calcareous soils to verify the following scientific hypothesis: soil colloids are organic-inorganic composites. As particle diameter decreases (from colloid particles to nanoparticles), the number of organic functional groups on the surface of soil colloids increases, and the type of clay minerals shifts towards finer clay particles, e.g. illite, resulting in increased specific surface area and decreased charge density, and thus enhanced suspension stability, meaning particle diameter influences the composition of soil colloidal fractions, thereby changing surface properties and suspension stability. The findings can have

important implications for predicting the environmental performances of colloids and colloid-facilitated nutrients, pollutes and pathogens in natural soil and water environment.

2. Materials and methods

2.1 Soil sampling

The study collected two surface soil samples (0–20 cm), Lou soil and Cinnamon soil, being the most common and characteristic calcareous soils, by mixing soils form 5–10 sampling points using a stainless-steel auger at Yangling District (38°18′14″ N and 108°2′30″ E), and Zhouzhi Country (34°8′8″ N and 108°3′10″ E), on the Guanzhong Plain, Shaanxi province, northwest China, respectively. Among these, Lou soil, as a unique calcareous soil, have formed on the basis of cinnamon soil through long-term anthropogenic maturation. According to World Reference Base for Soil Resources (WRB, IUSS Working Group WRB. 2022), the Lou soil and Cinnamon soil are classified as Hortic Endoanthric Anthrosols (Loamic, Luvic, Eutric, Calcic) and Calcic Protocalcic Calcisols (Loamic, Lixic, Humic), respectively. Both types of soil developed from loess parent material. The typical soil profile configuration for the tested Anthrosols is Ap1-Ap2-Bt-Bk-C, while for the Calcisols, it is Ah-Bt-Bk-C.

Soils samples were taken back to the laboratory for air-drying and sieving. The basic soil properties were determined based on standard methods. Soil pH was measured with a pH electrode, employing a solution-to-soil ratio of 2.5:1. Soil organic carbon (SOC) was determined using the $K_2Cr_2O_7$ oxidation method. The cation exchange capacity (CEC) of soil was measured with exchange method. The $CaCO_3$

content was determined by gasometric method. The free Fe/Al oxides were extracted by dithionite-citrate-bicarbonate (DCB) solution. The particle size distribution was measured using the laser diffractometer of Malvern Mastersizer 2000 (Malvern Instruments Ltd., UK). The pH of Anthrosols was 8.34 while it was 8.32 for Calcisols. The SOC of Anthrosols and Calcisols were 7.25 $g \cdot kg^{-1}$ and 9.22 $g \cdot kg^{-1}$, respectively. The CEC of Anthrosols and Calcisols were 25.9 $cmol \cdot kg^{-1}$ and 22.2 $cmol \cdot kg^{-1}$.The contents of $CaCO_3$ in Anthrosols and Calcisols were 51.7 $g \cdot kg^{-1}$ and 82.5 $g \cdot kg^{-1}$. The Free Fe/Al oxides content of Anthrosols and Calcisols were 22.8 $g \cdot kg^{-1}$ and 23.1 $g \cdot kg^{-1}$. The proportions of Sand (2–0.02 mm), Silt (0.02–0.002 mm) and Clay (<0.002 mm) in Anthrosols were 34.0%, 40.6% and 25.4% while those were 28.0%, 44.8% and 27.2% for the Calcisols.

2.2 Extraction of soil colloidal fractions in different size ranges

The soil colloidal particles were extracted based on the Stokes' law, and detailed procedures can be found in our previous publication (Hu et al., 2022). Briefly, 50 g of dry soil was weighed into a beaker containing 500 mL of distilled water, and put the suspension under sonication for an hour using the ultrasonic cell disrupter (XO-900D, Nanjing Xianou Instruments Corporation, China) while maintaining the temperature below 30°C. Afterwards, the suspension was transferred to a larger beaker and distilled water was added to make up the total volume of 5 L. The suspension was further dispersed using an electronic blade stirrer (JB-200, Shanghai Nanhui Huiming Apparatus, China) for one hour, before being sieved through sieve with a pore size of 53 μm, and the upper suspensions containing soil colloidal particles in different

diameters were collected by centrifugation. Based on the equation (1), centrifugation speed and time for colloidal particles of $d < 2$ μm, < 1 μm and < 100 nm were calculated and shown in Table S1.

$$t = \frac{\eta \lg \frac{R_2}{R_1}}{3.81 N^2 r^2 \Delta d} \quad (1)$$

in which, t is time for centrifugation (s); R_1 is the distance from the surface of the liquid to the center of the axis of the centrifuge, here is 5.7 cm; R_2 is distance from the particles to the center of the axis of the centrifuge, here is 10.5 cm; N (rev·s^{-1}) is the centrifuge speed; r (cm) is the desired colloidal particle radius; Δd is the difference in density between the soil particles (2.65 g·cm^{-3}) and water (1 g·cm^{-3}), while Δd is 1.65 g·cm^{-3}; η is the water viscosity coefficient, here is 0.00839 g·cm^{-1}·s^{-1} at 25 °C.

2.3 Characterization of soil colloidal fractions in different size ranges

The initial particle diameters of soil colloids were determined by a time-resolved dynamic light scattering (DLS) apparatus (Nanobrook Omni, Brookhaven, USA), each sample was measured 15 times to get the initial particle diameters. The organic carbon contents in soil colloids were determined by potassium dichromate external heating method and total carbon content was determined by elemental analyzer (Elementar Vario EL III, Germany). Total carbon and organic carbon are the averaged results of 3 measurements each. The inorganic carbon content was calculated by subtraction method (Wang et al., 2011). The clay mineralogy of soil colloids was determined by the XRD (Ultima-IV, Rigaku, Japan), and by comparing the intensity of the dominant X-ray diffraction peak of the soil mineral colloid to a standard mineral reference (Database

ICDD 2004), the relative percentage content of the minerals was determined. The specific surface areas of the soil colloids were measured by BET-N_2 method (ASAP 2460, Micromeritics instrument, USA). High-resolution spectra of C1s and O1s of soil colloids were acquired by X-ray photoelectron spectroscopy (XPS) (Thermo Scientific K-Alpha, USA) (Luo et al., 2019), and the Gaussian−Lorentzian curve-fitting program (XPSPEAK 4.1) was used to analyze the XPS spectra. The zeta potentials of soil colloids were measured by Zeta PALS equipped with a BI-ZTU Autotitrator (ZetaPALS, Brookhaven, USA) with 1 mmol·L^{-1} NaCl solution as the background electrolyte, and the pH range of colloidal suspension was set to 3–10 adjusted with 0.1 mol·L^{-1} HCl and NaOH. Each sample was measured six times to get the average zeta potential values. The concentrations of K^+, Na^+, Ca^{2+}, and Mg^{2+} in soil colloidal suspensions were measured by flame atomic absorption spectrophotometry (PinAAciie 900F, USA).

2.4 Aggregation kinetics of soil colloidal fractions

The aggregation kinetic curves of soil colloidal particles in different electrolytes were determined by time-resolved DLS measurements. The incident wavelength was 635 nm and the scattering angle was 90°. The stock colloidal suspensions with particle concentration of 200 mg·L^{-1} were mixed with electrolyte solutions with equal volume. The suspension pH was adjusted to 8.0, which was close to the pH value of natural soil with addition of 0.1 mol·L^{-1} HCl or NaOH before measurement. The chosen electrolyte concentrations for NaCl and $CaCl_2$ were 200–2000 and 2–20 mmol·L^{-1}. The effective diameter (D_h) of the mixed sample was automatically recorded every 2 min, and an aggregation kinetic curve was obtained in 30 min monitoring. According to generally

adopted by most research, the aggregation curve was determined only for one time without repetition (Chen and Elimelech, 2006; Mashayekhi et al., 2012; Zhu et al., 2014; Liu et al., 2018).

2.5 Calculation of critical coagulation concentration

According to the particle interaction theory, the aggregation kinetic curves under electrolyte conditions can be divided into reaction-limited aggregation (RLA) stage under low concentration which was affected by electrolyte conditions and diffusion-limited aggregation (DLA) stage under high concentration which was not affected by electrolyte concentration. The CCC is the critical electrolyte concentration when the aggregation process changes from the RLA state ($\alpha < 1$) to the DLA state ($\alpha = 1$). Attachment efficiency (α) represents the bonding probability of particle collisions and can be calculated for each electrolyte concentration by using equation 2, which allowed the curve of α as a function of electrolyte concentration to be plotted (Xu et al., 2020a; Hu et al., 2022).

$$\alpha_{\exp} = \frac{1}{W} = \frac{k_{11}}{\left(k_{11}\right)_{fast}} = \frac{\frac{1}{N_0}\left(\frac{\mathrm{d}a_h(t)}{\mathrm{d}t}\right)_{t\to 0}}{\frac{1}{\left(N_0\right)_{fast}}\left(\frac{\mathrm{d}a_h(t)}{\mathrm{d}_t}\right)_{t\to 0,\,fast}} \quad (2)$$

where D_h is the effective diameter of particles, t is the time (min); N_0 is the density of particles; K_{11} is the aggregation rate of RLA; $(K_{11})_{fast}$ is the aggregation rate of DLA. The intersection of RLA regime and DLA regime is the CCC.

The aggregation rates were calculated by the average of the last 5 effective diameters divided by the aggregation time at specific electrolyte concentration. The

fractal dimension in the DLA regime was obtained based on the method proposed by Wang et al. (2013).

$$D(t) = b * t^{n} + D_0 \quad (3)$$

in which, $D(t)$ is the colloidal effective diameter at time t (min), D_0 is the initial effective diameter of colloids, and b and n are constants determined by the aggregation curves. The fractal dimension is $d_f = 1/n$ in the DLA regime.

3. Results and discussion

3.1 Particle size and distribution characteristics of Anthrosol and Calcisol colloidal fractions

The average diameters of Anthrosol and Calcisol colloids were measured by time-resolved DLS, and the results were shown in Table 1. The number-weighted diameters for Anthrosol colloids of $d < 2$ μm were about 1.04 times of $d < 1$ μm, and about 1.84 times of d < 100 nm, respectively. The intensity-weighted diameters for Anthrosol colloids were 294.10~396.81 nm. For Calcisol colloidal fractions, the number-weighted diameters for colloids of $d < 2$ μm were about 1.07 times of $d < 1$ μm, and about 1.65 times of d < 100 nm, and the intensity-weighted diameters were 312.25~439.20 nm. The intensity-weighted diameters were generally higher than the number-weighted diameters, especially in polydisperse system (Xu et al., 2020b). The colloidal particles in the soil solution were in constant Brownian motion, upon illumination by light, these colloidal particles scatter light, causing variations in light intensity. This phenomenon allowed for the calculation of the effective diameter of the particles, which was the intensity-weighted diameter (Filella et al., 1997). Given that particle diameter is

proportional to the sixth power of light intensity. Consequently, in polydisperse systems where larger particles were present, the number-weighted diameter provided typically a more accurate representation of the true diameter of colloidal particles (Xu et al., 2015).

(*Insert Table 1 near here*)

From table 1, it can be seen that the average colloidal diameters of $d < 2$ μm were close to that of $d < 1$ μm, and they were both significantly higher than that of the nano-sized fraction. From the particle size distribution characteristics, it is clear that the size range indicated by the differences of D_{90} and D_{10} increased with intended particle diameter. For Anthrosol and Calcisol, 74.69% and 63.55% of all particles contained in the colloidal suspensions of $d < 100$ nm were actually less than 100 nm, respectively, indicating the complexity of soil colloidal particle irregularity.

3.2 Physiochemical properties and clay mineralogy of Anthrosol and Calcisol colloids

Table 2 shows the physiochemical properties of soil colloidal fractions. The yields of each colloidal fraction of Anthrosol were slightly larger than that of Calcisol, respectively. The yields of colloidal particles of $d < 2$ μm were about 1.3~1.4 times of $d < 1$ μm, and about 4.0~4.9 times of $d < 100$ nm, respectively. With the decreasing colloidal particle diameter, the total carbon content, organic carbon and inorganic carbon content all increased, suggesting the finer particles were richer in carbon. This tendency is in agreement with other publications (Zhang et al., 2021; Said-Pullicino et al., 2021; Hu et al., 2022). The specific surface areas for colloidal fractions of $d < 1$ μm

were largest of all, which may be related to the structures of formed clusters while drying the samples for observation under microscopy (Yu et al., 2017; Weissenberger et al., 2021). Furthermore, Anthrosol and Calcisol nanoparticles exhibited the lowest specific surface area. This phenomenon raised from Organic substances adsorb relatively little inorganic nitrogen (Li et al., 2013; Wilson et al., 2008). Therefore, However, to our knowledge, no other better method has been reported for measuring the specific surface area of natural nanoparticles.

(*Insert Table 2 near here*)

The clay mineralogy of Anthrosol and Calcisol colloidal fractions is shown in Table 3. Calcisol colloidal fractions were dominant by illite, kaolinite and chlorite while there was less chlorite in Anthrosol colloidal fractions. With the decrease of particle size, the content of illite increased and kaolinite content decreased. This tendency is in agreement with other publications (Chenu and Plante, 2006; Zhang et al., 2016). Among the dominant clay types, the size of illite is finer than kaolinite and chlorite (Weil and Brady, 2016), so its mass percentage was higher in the nano-sized fraction.

(*Insert Table 3 near here*)

3.3 Surface properties of Anthrosol and Calcisol colloids

The XPS spectra of soil colloidal fractions are shown in Fig. 1. From Fig. 1, it can be seen that the main C-containing functional groups were C–C/C-H/C=C, C–O, C=O, and COO- groups at 284.6, 286.2, 288.0 and 289.4 eV, respectively (Liang et al., 2020; Ding et al., 2023). The functional groups for colloidal particles of d < 100 nm were more abundant than those for colloids of d < 2 μm and d < 1 μm, while there were no

significant differences between colloids of $d < 2$ μm and $d < 1$ μm. With the decrease of colloidal particle diameter, the relative contents of oxygen-containing functional groups (C–O, C=O, COO-) gradually decreased. Specifically, the content decreased gradually from 32.01% in Lou colloids of $d < 2$ μm to 20.93% in Lou colloids of $d <$ 100 nm (Table S2). The functional groups of C–O and COO- gradually decreased until they eventually disappeared, more C=O groups were exposed to the surrounding air.

For Calcisol colloids (Fig. 1d, e, f), the relative contents of organic oxygen-containing functional groups for colloidal particles of $d < 2$ μm, $d < 1$ μm and $d < 100$ nm showed a different trend, compared with that in Anthrosol colloids. The relative contents of organic oxygen-containing functional groups gradually increased with the decrease of diameter. This trend was particularly pronounced in fraction of $d < 100$ nm, and contents of C–O and COO- were highly increased (Table S2).

(*Insert Figure 1 near here*)

Oxygen-containing functional groups of C–O, C=O and COO- are electronegative functional groups, hydroxyl and carboxyl groups can lose protons and make the surface of soil colloidal particles carry negative charges (Audette et al., 2021). Functional groups of C–O, C=O and COO- can affect the negative charges carried on the colloidal surface by forming hydrogen bonds, and their polarity can also affect the negative charges on the surface when O atom combines with C and H. The electrons will lean towards the O atom with stronger electronegativity, which also makes the colloidal surface carry negative charges (Tan et al., 2019). The contents and types of oxygen-containing functional groups are one of the main factors affecting colloid charge and aggregation.

The zeta potential values of different colloidal fractions at the pH range of 3–10

311 are shown in Fig. 2. Zeta potentials of the colloidal particles were negative, indicating
312 that they were negatively-charged. The zeta potentials of Anthrosol and Calcisol
313 colloidal particles were more negative with increasing solution pH, due to the
314 deprotonation of the surface (Moayedi and Kazemian, 2013; Dong et al., 2019).
315 Compared with the Calcisol colloids, the zeta potentials of Anthrosol colloidal particles
316 were more negative, due to Anthrosol possessed a higher surface charge density. For
317 Calcisol colloids, the differences among colloidal fractions were larger.

318 (*Insert Figure 2 near here*)

319 In general, zeta potential became more negative with increasing particle diameter.
320 When the pH changed from 3 to 10, for every pH unit increased, the zeta potential
321 values of Anthrosol colloids of $d < 2$ μm, < 1 μm, and < 100 nm would be increased by
322 2.14 mV, 2.09 mV and 1.89 mV; and for Calcisol colloids, those variation rates were
323 2.15 mV, 1.45 mV and 1.37 mV, respectively. Those data demonstrate that the charge
324 variability decreasing with the decreasing particle diameter. Song et al., (2019)
325 compared the zeta potential of wheat straw biochar nanoparticles (< 100 nm) and
326 colloidal particles (< 1000 nm), and found that the absolute values of colloidal particles
327 were larger at same pH, which was explained by the differences in the number of
328 surface carboxyl and hydroxyl groups. The zeta potential of colloidal particles is
329 proportional to charge density, which means that it is related to both charge quantity
330 and specific surface area (Hou et al., 2009). Therefore, the size effect of zeta potential
331 of Anthrosol and Calcisol colloidal particles is mainly related to the reduction of charge
332 density caused by larger specific surface area of nanoparticles (Xu et al. 2020b).

3.4 Aggregation kinetics curves of Anthrosol and Calcisol colloids in NaCl and $CaCl_2$ solutions

The aggregation kinetics of Anthrosol and Calcisol colloids in NaCl and $CaCl_2$ solutions are shown in Figs. S1 and S2. The aggregation process of soil colloids was divided into RLA and DLA stages. The RLA stages for Anthrosol colloids of $d < 2$ μm, $d < 1$ μm and $d < 100$ nm in NaCl solution were 0–80, 0–80 and 0–100 mmol·L^{-1}, respectively, during which repulsive forces existed between the particles and attachment did not occur on every collision. As the electrolyte concentration continued to increase, the solution entered into the DLA regime. At this point, attachment occurred with every collision between particles, and the aggregation rates were not affected by the electrolyte concentration. At last, the effective diameters of the formed clusters were stable at around 1600 nm. Figure S1b, d and f showed that the aggregation behaviors of Anthrosol colloids in $CaCl_2$ solution were similar to that in NaCl solution, and the corresponding $CaCl_2$ concentrations for Anthrosol colloids of $d < 2$ μm, $d < 1$ μm and $d < 100$ nm in RLA stage were about 0–1.5, 0–1.5 and 0–2 mmol·L^{-1}, respectively.

The aggregation kinetics of Calcisol colloids in NaCl and $CaCl_2$ solutions were similar to Anthrosol colloids (Fig. S2). The RLA stages for Calcisol colloids of $d < 2$ μm, $d < 1$ μm and $d < 100$ nm in NaCl solution were 0–100, 0–120 and 0–250 mmol·L^{-1}, and were about 0–1.8, 0–1.7 and 0–2 mmol·L^{-1} in $CaCl_2$ solution, respectively. The effective diameters of the clusters for Calcisol colloids were stabilized at about 1600 nm and 1800 nm in NaCl and $CaCl_2$ solutions, respectively.

Aggregation rates of soil colloids varied with particle diameters at the same

electrolyte concentration, which was particularly evident in RLA stage (Table 4). With decreasing particle diameter, the aggregation rates of Anthrosol and Calcisol colloids in 50 mmol·L^{-1} NaCl and 1 mmol·L^{-1} $CaCl_2$ solutions exhibited a corresponding decline. In addition, in 50 mmol·L^{-1} NaCl solution, the aggregation rates for Anthrosol colloids of d < 2 μm, d < 1 μm and d < 100 nm were about 2.17, 2.09 and 1.95 times those of Calcisol colloids, while the aggregation rates were about 1.46, 1.57 and 1.91 times those of Calcisol colloids in 1 mmol·L^{-1} $CaCl_2$ solution, respectively. Therefore, from table 4, the aggregation rates of Anthrosol and Calcisol colloids showed the size effect. From table 4, it could be observed that the fractal dimensions in NaCl solutions were largely higher than those in $CaCl_2$ solutions, suggesting a much denser structure (Meng et al., 2013). In other words, the formed structures in divalent solutions were more open.

(*Insert Table 4 near here*)

3.5 Suspension stability of Anthrosol and Calcisol colloids in NaCl and $CaCl_2$ solutions

The CCCs for Anthrosol colloids of d < 2 μm, d < 1 μm and d < 100 nm in NaCl solution were 80.40, 91.78 and 134.96 mmol·L^{-1}, respectively (Fig. 3a), and those for Calcisol colloids were 121.10, 126.50 and 292.86 mmol·L^{-1}, respectively (Fig. 3b). The CCCs increased with the decreasing particle diameter, indicating that the suspension stability of soil nanoparticles was stronger than those of colloidal particles.

(*Insert Figure 3 near here*)

In $CaCl_2$ solutions, the CCCs for Anthrosol colloids of d < 2 μm, d < 1 μm and d

377 < 100 nm were 1.61, 1.68 and 1.77 mmol·L^{-1}, respectively, and for Calcisol colloids,
378 those corresponding values were 1.90, 1.91 and 2.13 mmol·L^{-1} (Fig. 4). The CCCs in
379 $CaCl_2$ solutions also increased with the decreasing particle size. The contents of K^+,
380 Na^+, Ca^{2+} and Mg^{2+} in Anthrosol and Calcisol colloidal suspensions decreased with the
381 decreasing colloidal particle diameter (Table S3), which was mainly due to the dilution
382 effect during the extraction process. Furthermore, Table S3 showed that the soluble
383 cation contents were rather low, and their effects on the CCCs of soil colloids could be
384 neglected.

385 (*Insert Figure 4 near here*)

386 Based on Figs. 3 and 4, 3 mmol·L^{-1} $CaCl_2$ solution could cause fast aggregation
387 of soil colloidal particles, while it required at least 80 mmol·L^{-1} NaCl solution for
388 comparable aggregation rate, indicating that the shielding effect of divalent cations on
389 negative charges of colloids was stronger than that of monovalent cations. The
390 quantitative calculation results showed that the CCC ratios of monovalent ion and
391 divalent ion system were between 25.64 and 27.09, which conformed to the Schulze-
392 Hardy rule (Baalousha, 2017).

393 For each type of the soil colloids, the higher the absolute zeta potential values of
394 colloidal particles, the more negative charges carried on the surface, and the higher the
395 stability (CCCs) of suspension. For the same particle diameter, e.g. d < 100 nm, the
396 absolute zeta potentials of Anthrosol colloids were larger (Fig. 2) while the
397 corresponding CCC was lower (Figs. 3 and 4). Study on the stability of biochar
398 nanoparticles showed that the absolute values of zeta potentials could not be used to

399 directly explain the stability difference among biochar nanoparticles from different
400 feedstock materials but could explain the influences of solution conditions on the
401 stability of biochar nanoparticles derived from the same feedstock material (Xu et al.,
402 2020a).

403 The CCCs of Anthrosol and Calcisol colloids increased with decreasing diameter;
404 that is, the CCCs of Anthrosol and Calcisol colloids both showed the size effects. Hsu
405 and Kuo (1995) demonstrated that the CCCs would generally decrease with the
406 increasing particle diameter because smaller particles possess thicker double electric
407 layers and higher electrolyte concentration is needed to neutralize charges on the
408 surface, which were consistent with the results of Anthrosol and Calcisol colloids. The
409 above explanation by Hsu and Kuo (1995) was derived from homogenous particles
410 whose composition does not change with particle diameter. The results of this paper
411 show that, for those two alkaline soils being such heterogeneous materials, when the
412 organic matter contents and mineral types changed with colloidal particle diameter, the
413 CCCs in monovalent and divalent solutions also decreased with increasing particle
414 diameter.

415 In this paper, the organic matter contents of soil nanoparticles were the highest, so
416 the CCCs were the largest, which were 1.7 and 2.4 times of the corresponding colloidal
417 particles of $d < 2$ μm. The suspension stability of different clay minerals has been
418 reported to vary with the mineralogical structure. The CCC of illite (≈100 mM) in
419 NaCl solution was significantly higher than that of kaolinite (≈20 mM) (Jiang et al.,
420 2012; Xu et al., 2017), indicating that the stability of illite suspensions is significantly

higher than that of kaolinite. So another possible reason for the higher stability of soil nanoparticles is the increase of illite content and the decrease of kaolinite content. Therefore, the differences in organic matter contents and clay mineralogy are the fundamental reasons for the differences in colloidal suspension stability behind the size effects of Anthrosol and Calcisol colloids.

4. Conclusion

This study obtained soil colloidal fractions with three different particle sizes from Anthrosol and Calcisol using high-speed centrifugation and revealed the particle size effects on the soil constitutes, surface properties, and aggregation behavior of heterogeneous soil colloids. The results showed that, compared to coarse colloids ($d <$ 2 μm and $d <$ 1 μm), the organic carbon contents of Anthrosol and Calcisol nanoparticles were higher, at 27.38 $g \cdot kg^{-1}$ and 28.31 $g \cdot kg^{-1}$, respectively, approximately twice and three times that of the coarse colloids and the bulk soils, indicating that nanoparticles exhibit a strong potential for carbon sequestration. The absolute zeta potential values of soil nanoparticles decreased with decreasing average particle diameter, indicating a reduction in charge density. Anthrosol and Calcisol nanoparticles exhibited greater suspension stability in NaCl and $CaCl_2$ solutions. On one hand, this was due to the increased thickness of the double electric layer on the surface of soil nanoparticles, resulting in stronger repulsive forces between particles; on the other hand, it was due to the presence of more illite, which has higher CCC compared to other clay minerals. In conclusion, for such a highly heterogeneous system as soil, the size effects on soil colloidal suspension stability are strongly influenced by

variations driven by essentially mineral composition. Future studies should further explore the mechanisms underlying the size effects of the typical soils on particle interactions, coagulation, and transport behaviors under environmentally relevant conditions.

Acknowledgments

This work was supported by Natural Science Foundation of Shaanxi Province (2023-JC-YB-263) and the National Natural Science Foundation of China (41701261), and the Fundamental Research Funds for the Central Universities (2452020165).

Author Contributions

Conceptualization, Xu, C.Y., Geng, Z.C., and Hu, F.N.; methodology, Xu, C.Y.; software, Yan, Y.Y.; formal analysis, Liu, J.J.; investigation, Zhang, X.R.; resources, Yan, Y.Y.; writing—original draft, Yan, Y.Y.; writing—review and editing, Xu, C.Y., and Hu, F.N.; visualization, Xu, C.Y., and Yan, Y.Y.; funding acquisition, Xu, C.Y., Geng, Z.C. and Hu, F.N.. All authors have read and agreed to the published version of the manuscript.

Declaration of Interest Statement

The authors declare that they have no known competing financial interests or personal relationships that could have appeared to influence the work reported in this paper.

References

Audette, Y., Congreves, K.A., Schneider, K., Zaro, G.C., Nunes, A.L.P., Nunes, A.L.P., Zhang, H.J., Voroney, R.P.: The effect of agroecosystem management on the distribution of C functional groups in soil organic matter: A review. Biol. Fertil. Soils. 57, 881–894, 2021.

Baalousha, M.: Aggregation and disaggregation of iron oxide nanoparticles: Influence of particle concentration, pH and natural organic matter. Sci. Total Environ. 407(6), 2093–2101, 2009.

Baalousha, M.: Effect of nanomaterial and media physicochemical properties on nanomaterial aggregation kinetics. NanoImpact. 6, 55–68, 2017.

Cárdenas, J.P., Santiago, A., Tarquis, A.M., Losada, J.C., Borondo, F., Benito, R.M.: Soil porous system as heterogeneous complex network. Geoderma. 160(1), 13–21, 2010.

Chen, K.L., Elimelech, M.: Aggregation and deposition kinetics of Fullerene (C_{60}) nanoparticles. Langmuir 22, 10994–11001, 2006.

Chenu, C., Plante, A.F.: Clay-sized organo-mineral complexes in a cultivation chronosequence: revisiting the concept of the‘primary organo-mineral complex’. Eur J Soil Sci. 57(4), 596–607, 2006.

Ding, W., Liang, H.X., Zhang, H.W., Sun, H., Geng, Z.C., Xu, C.Y.: A cellulose/bentonite grafted polyacrylic acid hydrogel for highly-efficient removal of Cd(II). J. Water Process. Eng. 51, 103414, 2023.

Dong, S.N., Zeng, Z., Cai, W.W., Zhou, Z.Y., Dou, C.B., Liu, H., Xia, J.H.: The zeta potentials of g-C_3N_4 nanoparticles: Effect of electrolyte, ionic strength, pH, and humic acid. J. Nanopart Res. 21, 233, 2019.

Filella, M., Zhang, J.W., Newman, M.E., Buffle, J.: Analytical applications of photon correlation spectroscopy for size distribution measurements of natural colloidal suspensions: capabilities and limitations. Colloid Surf. A. 120(1–3), 27–46, 1997.

He, Y.T., Wan, J., Tokunaga, T.: Kinetic stability of hematite nanoparticles, The effect of particle sizes. J. Nanopart Res. 10, 321–332, 2008.

Hou, J., Li, H., Zhu, H.L.,Wu, L.S.: Determination of clay surface potential, a more reliable approach. Soil Sci Soc Am J. 73(5), 1658–1663, 2009.

Hsu, J.P., Kuo, Y.C.: An Extension of the Schulze-Hardy Rule to Asymmetric Electrolytes. J. Colloid Interface Sci. 171(1), 254–255, 1995.

Hu, N., Xu, C.Y., Geng, Z.C., Hu, F.N., Li, Q.R., Ma, R.T., Wang, Q.: The interplay of particle properties and solution chemistry on aggregation kinetics of soil nanoparticles. J Soils Sediments. 22, 1761–1772, 2022.

IUSS Working Group WRB. World Reference Base for Soil Resources. International soil classification system for naming soils and creating legends for soil maps. 4th edition. International Union of Soil Sciences (IUSS), Vienna, Austria. 2022.

Jiang, C.L., Séquaris, J.M., Vereecken, H., Klumpp, E.: Effects of inorganic and organic anions on the stability of illite and quartz soil colloids in Na-, Ca- and mixed Na-Ca systems. Colloids Surf. A. 415, 134–141, 2012.Lead, J.R., Wilkinson, K.J.: Aquatic Colloids and Nanoparticles: Current Knowledge and Future Trends.

Environ. Chem. 3(3), 159–171, 2006.

Li, S.X., Luo, Y.M., Zhang, H.B., Huang, Y.J., Li, Z., Wei, J.: Arsenic forms in various particle-size fractions of red soil-Chemical fractionation and speciation using XANES analysis. Acta Scientiae Circumstantiae. 31(12), 2733–2739, 2011.

Li, W. Y., Zhu, X.Y., He, Y., Xing, B. S., Xu, J.M.: Enhancement of water solubility and mobility of phenanthrene by natural soil nanoparticles. Environ Pollut. 176, 228–233, 2013.

Liang, H.X., Sun, R.R., Song, B., Sun, Q.Q., Peng, P., She, D.: Preparation of nitrogen-doped porous carbon material by a hydrothermal-activation two-step method and its high-efficiency adsorption of Cr(VI). J. Hazard. Mater. 387, 121987, 2020.

Liu, G., Zheng, H., Jiang, Z., Zhao, J., Wang, Z., Pan, B., Xing, B.: Formation and physicochemical characteristics of nano biochar: insight into chemical and colloidal stability. Environ. Sci. Technol. 52(18), 10369–10379, 2018.Luo, J.J., Niu, Q., Jin, M.C., Cao, Y.A., Ye, L.R., Du, R.P.: Study on the effects of oxygen-containing functional groups on Hg^0 adsorption in simulated flue gas by XAFS and XPS analysis. J. Hazard. Mater. 376(15), 21–28, 2019.

Mashayekhi, H., Ghosh, S., Du, P., Xing, B.: Effect of natural organic matter on aggregation behavior of C60 fullerene in water. J. Colloid Interf. Sci. 374(1), 111–117, 2012.

Mayordomo, N., Degueldre, C., Alonso, U., Missana, T.: Size distribution of FEBEX bentonite colloids upon fast disaggregation in low-ionic strength water. Clay Miner. 51(2), 213–222, 2016.

529 Meng, Z.Y., Hashmi, S.M., Elimelech, M.: Aggregation rate and fractal dimension of
530 fullerene nanoparticles via simultaneous multiangle static and dynamic light
531 scattering measurement. J. Colloid Interface Sci. 392, 27–33, 2013.
532 Moayedi, H., Kazemian, S.: Zeta potentials of suspended humus in multivalent cationic
533 saline solution and its effect on electro-osomosis behavior. J. Dispers Sci. Technol.
534 34(2), 283–294, 2013.
535 Said-Pullicino, D., Giannetta, B., Demeglio, B., Missong, A., Gottselig, N., Romani,
536 M., Bol, R., Klumpp, E., Celi, L.: Redox-driven changes in water-dispersible
537 colloids and their role in carbon cycling in hydromorphic soils. Geoderma. 385,
538 114894, 2021.
539 Schäfer, T., Huber, F., Seher, H., Missana, T., Alonso, U., Kumke, M., Eidner, S., Claret,
540 F., Enzmann, F.: Nanoparticles and their influence on radionuclide mobility in
541 deep geological formations. Appl. Geochemistry. 27(2), 390–403, 2012.
542 Song, B.Q., Chen, M., Zhao, L., Qiu, H., Cao, X.D.: Physicochemical property and
543 colloidal stability of micron- and nano-particle biochar derived from a variety of
544 feedstock sources. Sci. Total Environ. 661, 685–695, 2019.
545 Sun, Y.L., Pan, D.Q., Wei, X.Y., Xian, D.F., Wang, P., Hou, J.J.: Insight into the stability
546 and correlated transport of kaolinite colloid: Effect of pH, electrolytes and humic
547 substances. Environ. Pollut. 266, 115189, 2020.
548 Tan, Z.X., Yuan, S.N., Hong, M.F., Zhang, L.M., Huang, Q.Y.: Mechanism of negative
549 surface charge formation on biochar and its effect on the fixation of soil Cd. J.
550 Hazard. Mater. 384, 121370, 2019.

551 Tang, Y., Li, H., Liu, X.M., Zhu, H.L., Tian, R.: Unraveling the size distributions of
552 surface properties for purple soil and yellow soil. J Environ Sci (China). 32, 81–
553 89, 2015.
554 Tsao, T.M., Chen, Y.M., Sheu, H., Tzou, Y.M., Chou, Y.M., Wang, M.K.: Separation
555 and identification of soil nanoparticles by conventional and synchrotron X-ray
556 diffraction. Appl. Clay Sci. 85, 1–7, 2013.
557 Tsao, T.M., Chen, Y.M., Wang, M.K., Huang, P.M.: Structural transformation and
558 physicochemical properties of environmental nanoparticles by comparison of
559 various particle-size fractions. Soil Sci Soc Am J. 75(2), 533–541, 2011.
560 Wang, L.F., Wang, L.L., Ye, X.D., Li, W.W., Ren, X.M., Sheng, G.P., et al.: Coagulation
561 kinetics of humic aggregates in mono-and divalent electrolyte solutions. Environ.
562 Sci. Technol. 47(10), 5042–5049, 2013.
563 Wang, Q.R., Li, Y.C., Wang, Y.: Optimizing the weight loss-on-ignition methodology
564 to quantify organic and carbonate carbon of sediments from diverse sources.
565 Environ. Monit. Assess. 174, 241–257, 2011.
566 Wei, X.Y., Pan, D.Q., Xu, Z., Xian, D.F., Li, X.L., Tan, Z.Y., Liu, C.L., Wu, W.S.:
567 Colloidal stability and correlated migration of illite in the aquatic environment:
568 The roles of pH, temperature, multiple cations and humic acid. Sci. Total Environ.
569 768, 144174, 2021.
570 Weil, R.R., Brady, N.C.: The Nature and Properties of Soils, Global Edition. Pearson
571 Education Limited. 2016.
572 Weissenberger, G., Henderikx, R.J., Peters, P.J.: Understanding the invisible hands of

573 sample preparation for cryo-EM. Nat. Methods. 18(5), 463–471, 2021.
574 Wilson, M. A., Tran, N. H., Milev, A. S., Kannangara, G. S. K., Volk, H.: Nanomaterials
575 in soils. Geoderma. 146, 291–302, 2008.
576 Won, J., Burns, S.E.: Role of Immobile Kaolinite Colloids in the Transport of Heavy
577 Metals. Environ. Sci. Technol. 52(5): 2735–2741, 2018.
578 Xu, C.Y., Deng, K.Y., Li, J.Y., Xu, R.K.: Impact of environmental conditions on
579 aggregation kinetics of hematite and goethite nanoparticles. J. Nanopart Res. 17,
580 394, 2015.
581 Xu, C.Y., Li, Q.R., Geng, Z.C., Hu, F.N., Zhao, S.W.: Surface properties and suspension
582 stability of low–temperature pyrolyzed biochar nanoparticles: Effects of solution
583 chemistry and feedstock sources. Chemosphere. 259, 127510, 2020a.
584 Xu, C.Y., Xu, R.K., Li, J.Y., Deng, K.Y.: Phosphate-induced aggregation kinetics of
585 hematite and goethite nanoparticles. J. Soils Sediments. 17, 352–363, 2017.
586 Xu, C.Y., Zhou, T.T., Wang, C.L., Liu, H.Y., Zhang, C.T., Hu, F.N., Zhao, S.W., Geng,
587 Z.C.: Aggregation of polydisperse soil colloidal particles: Dependence of
588 Hamaker constant on particle size. Geoderma. 359, 113999, 2020b.
589 Xu, Z., Pan, D.Q., Sun, Y.L., Wu, W.S.: Stability of GMZ bentonite colloids:
590 Aggregation kinetic and reversibility study. Appl. Clay Sci. 161, 436–443. 2018.
591 Yin, X.Q., Gao, B., Ma, L.Q., Saha, U.K., Sun, H.M., Wang, G.D.: Colloid-facilitated
592 Pb transport in two shooting-range soils in Florida. J. Hazard. Mater. 177(1–3),
593 620–625, 2010.
594 Yu, X., Fu, Y., Lu, S.: Characterization of the pore structure and cementing substances

595 of soil aggregates by a combination of synchrotron radiation X-ray micro–
596 computed tomography and scanning electron microscopy. Eur. J. Soil Sci. 68(1),
597 66–79, 2017.
598 Zhang, Q., Bol, R., Amelung, W., Missong, A., Siemens, J., Mülder, I.: Water
599 dispersible colloids and related nutrient availability in Amazonian Terra Preta soils.
600 Geoderma. 397, 115103, 2021.
601 Zhang, Z.Y., Huang, L., Liu, F., Wang, M.K., Fu, Q.L., Zhu, J.: Characteristics of clay
602 minerals in soil particles of two Alfisols in China. Appl. Clay Sci. 120, 51–60,
603 2016.
604 Zhou, D.X., Ji, Z.X., Jiang, X.M., Dunphy, D.R., Brinker, J., Keller A.A.: Influence of
605 material properties on TiO_2 nanoparticle agglomeration. PLoS One. 8(11), e81239,
606 2013.
607 Zhu, X., Chen, H., Li, W., He, Y., Brookes, P.C., Xu, J.: Aggregation kinetics of natural
608 soil nanoparticles in different electrolytes. Eur. J. Soil Sci. 65(2), 206–217, 2014.
609
610

Table captions

Table 1 The average diameters and distribution patterns of soil colloids.

Table 2 The physiochemical properties of soil colloids.

Table 3 The dominant clay minerals of soil colloidal fractions (shown in mass fraction, %).

Table 4 The aggregation rates of soil colloids.

618 **Table 1** The average diameters and distribution patterns of soil colloids

Soil type	Colloidal fractions	Number-weighted diameter (nm)	Intensity-weighted diameter (nm)	D_{10} (nm)	D_{90} (nm)
Anthrosol	d < 2 μm	133.16 ± 24.28	396.81 ± 12.34	71.53	232.49
	d < 1 μm	127.84 ± 20.29	371.45 ± 11.88	67.64	219.87
	d < 100 nm	72.47 ± 7.04	294.10 ± 15.80	38.74	136.72
Calcisol	d < 2 μm	141.23 ± 24.33	439.20 ± 12.72	78.29	244.97
	d < 1 μm	131.67 ± 15.77	372.07 ± 8.23	75.84	231.64
	d < 100 nm	85.48 ± 16.93	312.25 ± 33.58	47.84	158.99

619 Note: D_{10}, D_{50} and D_{90} represent diameter of particles with a cumulative distribution of 10%, 50% and
620 90%, respectively.
621

622 **Table 2** The physiochemical properties of soil colloids

Soil type	Colloidal fractions	Yield (%)	Total carbon content ($g \cdot kg^{-1}$)	Organic carbon content ($g \cdot kg^{-1}$)	$CaCO_3$ content ($g \cdot kg^{-1}$)	Specific surface area ($m^2 \cdot g^{-1}$)
Anthrosol	$d < 2$ μm	25.12	20.90 ± 0.30	10.90 ± 1.29	10.00	65.37
	$d < 1$ μm	18.76	20.65 ± 0.15	10.91 ± 0.43	9.74	72.99
	$d < 100$ nm	6.32	58.25 ± 0.35	27.38 ± 0.21	30.87	45.28
Calcisol	$d < 2$ μm	23.17	24.00 ± 0.30	11.66 ± 0.60	12.34	49.99
	$d < 1$ μm	16.20	22.30 ± 0.20	12.76 ± 0.11	9.54	61.88
	$d < 100$ nm	4.70	76.30 ± 0.40	28.31 ± 0.15	47.99	34.53

623

624 **Table 3** The dominant clay minerals of soil colloidal fractions (shown in mass fraction, %)

Soil type	Colloidal fractions	Illite	Kaolinite	Chlorite	Vermiculite
Anthrosol	$d < 2$ μm	34	23	4	9
	$d < 1$ μm	30	22	7	11
	$d < 100$ nm	37	14	16	3
Calcisol	$d < 2$ μm	24	22	29	16
	$d < 1$ μm	31	19	25	12
	$d < 100$ nm	37	16	17	5

625

626 **Table 4** The aggregation rates of soil colloids

Soil type	Colloidal fractions	Aggregation rate		Fractal dimension	
		In 50 mmol·L^{-1} NaCl (nm·min^{-1})	In 1 mmol·L^{-1} $CaCl_2$ (nm·min^{-1})	Na	Ca
Anthrosol	d < 2 μm	19.46	12.01	1.69 ± 0.19	1.33 ± 0.26
	d < 1 μm	14.91	11.48	1.75 ± 0.06	1.52 ± 0.19
	d < 100 nm	7.72	9.97	1.71 ± 0.26	1.68 ± 0.13
Calcisol	d < 2 μm	8.98	8.22	1.30 ± 0.17	1.36 ± 0.17
	d < 1 μm	7.15	7.33	1.71 ± 0.24	1.30 ± 0.31
	d < 100 nm	3.95	5.22	1.52 ± 0.22	1.58 ± 0.19

627

628 **Figure captions**

629 **Fig. 1.** The photoelectron spectrum C1s and O1s peak diagram of Anthrosol and
630 Calcisol colloids. C1s of Anthrosol colloids, a. $d < 2$ μm, b. $d < 1$ μm, c. $d < 100$ nm;
631 C1s of Calcisol colloids, d. $d < 2$ μm, e. $d < 1$ μm, f. $d < 100$ nm; O1s of Anthrosol
632 colloids, g. $d < 2$ μm, h. $d < 1$ μm, i. $d < 100$ nm; O1s of Calcisol colloids, j. $d < 2$ μm,
633 k. $d < 1$ μm, l. $d < 100$ nm.

634 **Fig. 2.** The zeta potential of Anthrosol (a) and Calcisol (b) colloids of $d < 2$ μm, < 1 μm,
635 and < 100 nm at different pH

636 **Fig. 3.** The CCCs of Anthrosol (a) and Calcisol (b) colloids of $d < 2$ μm, < 1 μm, and <
637 100 nm in NaCl solution

638 **Fig. 4.** The CCC of Anthrosol (a) and Calcisol (b) colloids of $d < 2$ μm, < 1 μm, and <
639 100 nm in $CaCl_2$ solution

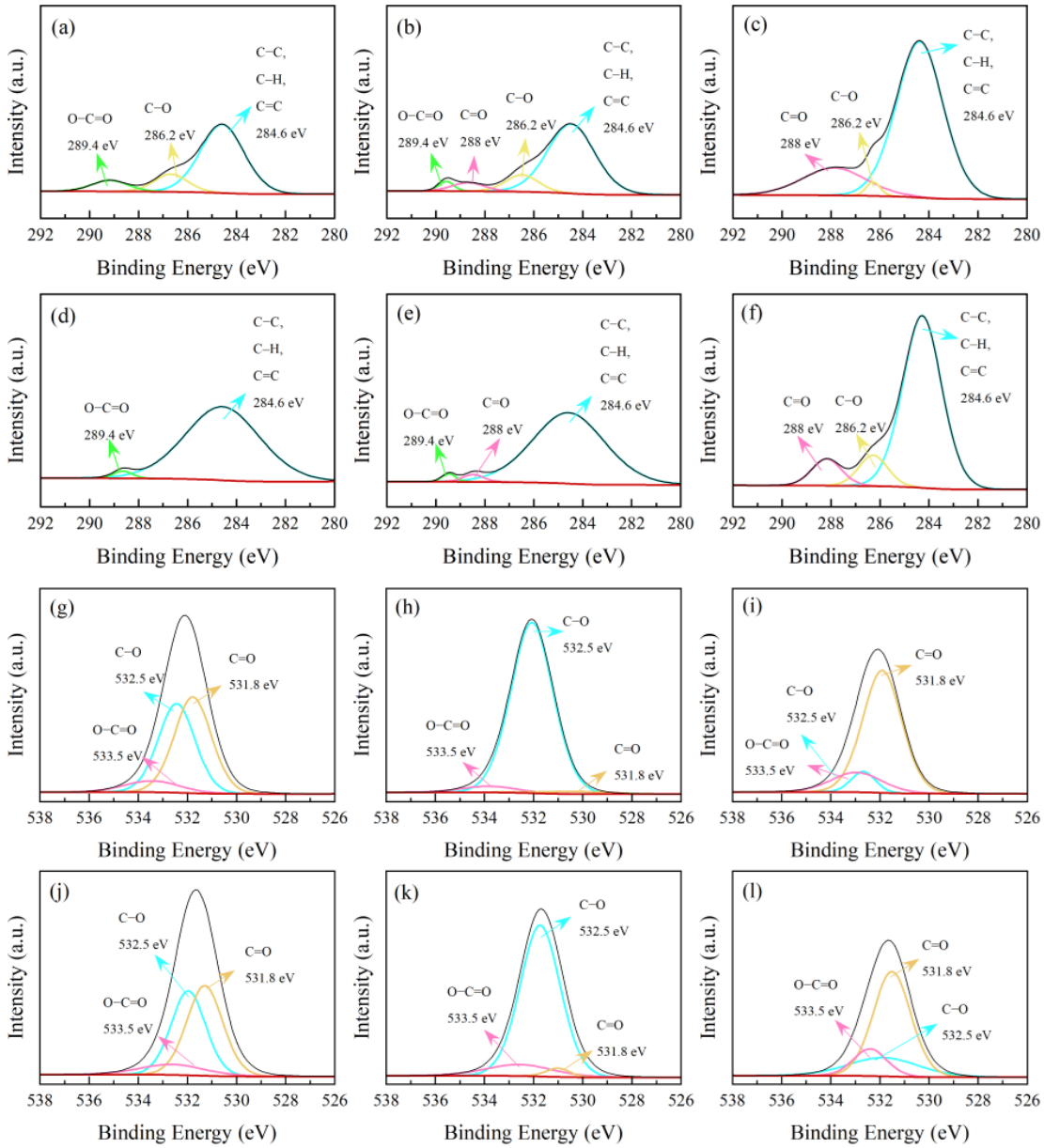

Fig. 1 The photoelectron spectrum C1s and O1s peak diagram of Anthrosol and Calcisol colloids. C1s of Anthrosol colloids, (a). $d < 2$ μm, (b). $d < 1$ μm, (c). $d < 100$ nm; C1s of Calcisol colloids, (d). $d < 2$ μm, (e). $d < 1$ μm, (f). $d < 100$ nm; O1s of Anthrosol colloids, (g). $d < 2$ μm, (h). $d < 1$ μm, (i). $d < 100$ nm; O1s of Calcisol colloids, (j). $d < 2$ μm, (k). $d < 1$ μm, (l). $d < 100$ nm.

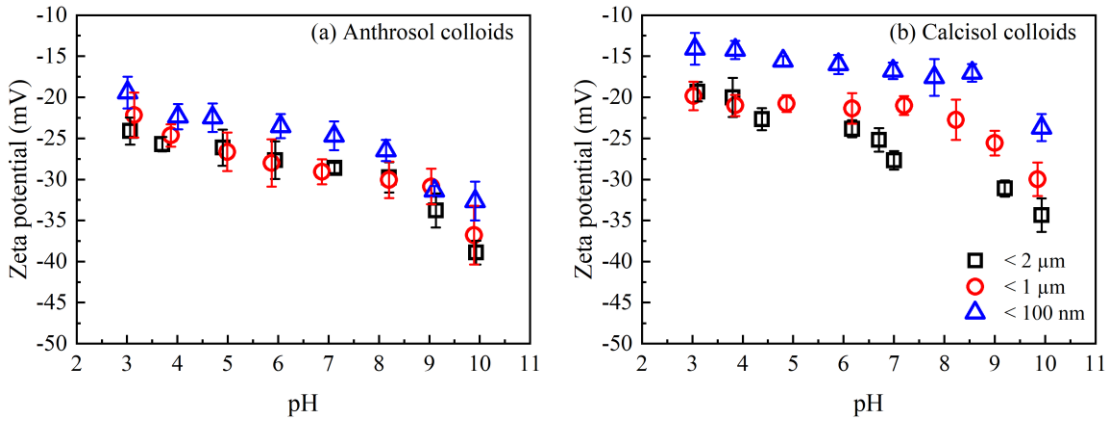

647

648 **Fig. 2** The zeta potential of Anthrosol (a) and Calcisol (b) colloids of *d* < 2 μm, < 1 μm, and <
649 100 nm at different pH

650

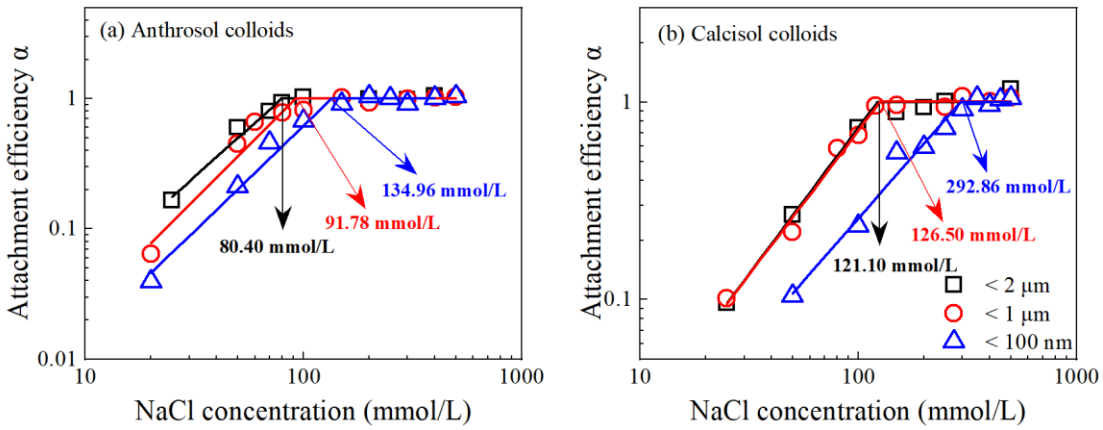

651
652

653 **Fig. 3** The CCCs of Anthrosol (a) and Calcisol (b) colloids of d < 2 μm, < 1 μm, and < 100
654 nm in NaCl solution

655

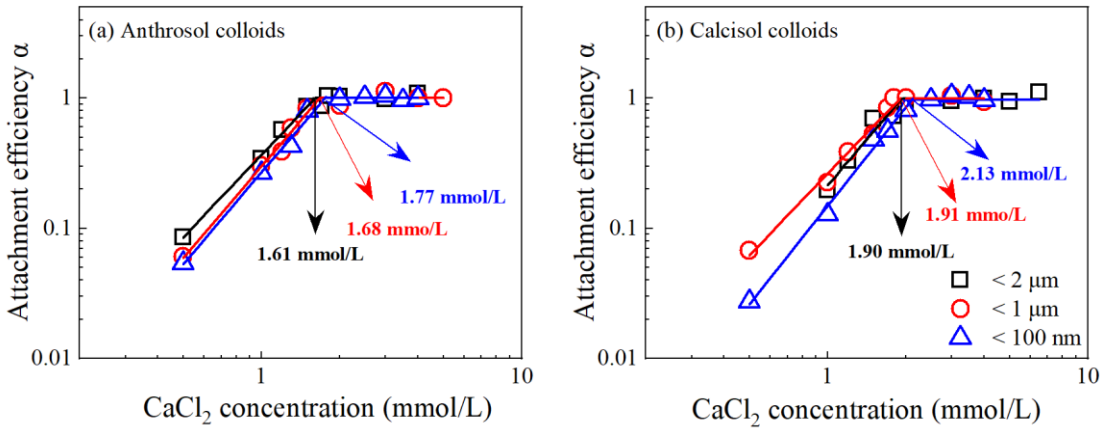

656

657 **Fig. 4** The CCC of Anthrosol (a) and Calcisol (b) colloids of d < 2 μm, < 1 μm, and < 100 nm

658 in $CaCl_2$ solution。